remote sensing

MDPI

Article

Impacts of Permafrost Degradation on the Water Conservation Function in the Three-River Source Region of the Qinghai–Tibet Plateau

Wei Bai [1,2,†], Chunyu Wang [1,2,†], Wenyan Liu [3], Guowei Zhang [1,2], Yixuan Yang [1,2], Qingyue Wang [1,2] and Zeyong Gao [3,*]

[1] School of Environmental and Municipal Engineering, Lanzhou Jiaotong University, Lanzhou 730070, China; baiwei@lzjtu.edu.cn (W.B.); 12241137@stu.lzjtu.edu.cn (C.W.); 12251168@stu.lzjtu.edu.cn (G.Z.)
[2] Engineering Research Center of Water Resource Comprehensive Utilization in Cold and Arid Regions, Ministry of Education, Lanzhou 730070, China
[3] Key Laboratory of Cryospheric Science and Frozen Soil Engineering, Northwest Institute of Eco-Environment and Resources, Chinese Academy of Sciences, Lanzhou 730000, China; liuwenyan24@mails.ucas.ac.cn
* Correspondence: gaozy@lzb.ac.cn
† These authors contributed equally to this work.

Highlights

What are the main findings?

- Water conservation increased across the TRSR (1990–2020), showing a southeast–northwest gradient, dominated by precipitation and its interaction with ALT.
- Water conservation shows a nonlinear response to active layer thickening, with a threshold around 1.77 m and a delayed response of ~5–7 years, varying markedly across space.

What are the implications of the main findings?

- Incorporating permafrost dynamics is critical for accurately assessing and projecting water conservation in alpine permafrost regions.
- Identified ALT thresholds and lags inform permafrost-sensitive area identification and adaptive water resource and ecological engineering management.

Abstract

As a major water conservation region and ecological security barrier in China, the Three-River Source Region (TRSR) of the Qinghai–Tibet Plateau (QTP) is underlain by extensive permafrost. However, how permafrost degradation alters regional water conservation, particularly the existence of critical thresholds and time-lagged responses, remains insufficiently understood. To clarify these issues, spatiotemporal variations in water conservation (1990–2020) were quantified, and their nonlinear, lagged, and spatially heterogeneous responses to active layer thickness (ALT) were assessed. Using multi-source remote sensing and in situ observations from 1990 to 2020, spatiotemporal variations in water conservation were quantified with the Integrated Valuation of Ecosystem Services and Tradeoffs (InVEST) model, and responses to permafrost degradation were examined by integrating Sen's slope, GeoDetector, geographically weighted regression (GWR), and structural equation modeling (SEM) methods. The results showed that water conservation increased overall during 1990–2020 and exhibited a pronounced southeast–northwest gradient (higher in the southeast and lower in the northwest); the rates of change in the Lancang, Yellow, and Yangtze headwaters were 63.5, 56.5, and 31.0 mm a^{-1}, respectively. GeoDetector results indicate that precipitation was the dominant control on the spatial heterogeneity

Check for updates

Academic Editor: Konstantinos X. Soulis

Received: 7 January 2026
Revised: 13 February 2026
Accepted: 13 February 2026
Published: 16 February 2026

Copyright: © 2026 by the authors. Licensee MDPI, Basel, Switzerland. This article is an open access article distributed under the terms and conditions of the Creative Commons Attribution (CC BY) license.

of water conservation (q = 0.704), and its interaction with active layer thickness (ALT) further increased explanatory power (q = 0.736). ALT also interacted with vegetation (q = 0.224) and topography (q = 0.157), suggesting that permafrost effects are modulated by vegetation condition and topographic setting in addition to water inputs. Piecewise regression identified a potential threshold at ALT = 1.77 m, indicating a shift in the ALT–water conservation relationship across this threshold. A 5–7-year lag in the response of water conservation to ALT was also detected, particularly apparent in continuous permafrost zones. Overall, water conservation exhibits a clear southeast–northwest gradient and a delayed response to ALT changes. In addition, the response exhibits clear spatial clustering, with the strongest sensitivity observed in areas with ice-rich permafrost overlain by alpine meadow, and a potential ALT breakpoint further suggests nonlinear permafrost–water conservation coupling.

Keywords: Three-River Source Region; permafrost degradation; water conservation function; InVEST model; spatiotemporal heterogeneity; critical threshold

1. Introduction

The water conservation function refers to the ability of ecosystems to intercept rainfall through the canopy, retard overland flow within the litter layer, and retain precipitation via roots and soil pore networks. By enhancing soil infiltration capacity and soil water storage, this function regulates hydrological processes including soil moisture buffering, attenuation of surface runoff, and groundwater recharge, and it also influences atmospheric moisture cycling through evapotranspiration [1]. As a fundamental ecosystem service [2], the water conservation function is tightly linked to watershed runoff processes and the spatiotemporal allocation of water resources and thus has strategic significance for safeguarding regional ecological security, water security, and socio-economic sustainability [3]. In addition, ecosystem water conservation is often coupled with water quality regulation, as vegetation and soils intercept sediment [4] and facilitate the uptake and degradation of pollutants [5], thereby supporting the safety of supplied water quality [6]. In alpine regions, this function is further constrained by cryospheric controls on soil thermal and hydraulic regimes [7]. Located in the interior of the QTP, the Three-River Source Region (TRSR) is a key ecological security barrier in China [8] and plays a central role in water conservation, biodiversity maintenance, and climate regulation [9]. The previous study indicated that the annual mean volume of water delivered downstream from the TRSR increased by nearly 10 billion m^3 during 2016–2020 [10], mainly due to increasing precipitation and enhanced cryospheric meltwater contributions under warming [11]. Permafrost is widespread across the TRSR, and intensified warming in recent decades has made the TRSR one of the areas on the QTP experiencing the most pronounced permafrost degradation [12]. Permafrost degradation is represented here by long-term ALT increase, a widely used regional-scale indicator of permafrost thaw that may also be locally influenced by human activities. Continued increases in ALT can degrade permafrost as a "solid water reservoir" by disrupting its water-holding structure [13] and by altering precipitation partitioning among surface runoff, shallow storage, and deep drainage through enhanced meltwater infiltration losses [14]. These hydrological shifts may further propagate via coupled biogeochemical and ecological processes, including organic matter mineralization and retrogressive vegetation succession [15], thereby generating cascading impacts on the water conservation function.

Previous studies have quantified spatiotemporal variations in water conservation and identified precipitation as a primary driver in the TRSR. However, the role of permafrost degradation especially potential threshold behavior and time-lagged responses remains insufficiently resolved. Jiang et al. (2016) systematically evaluated changes in regional ecosystem services using the InVEST model and reported that inter-annual fluctuations in water conservation are mainly controlled by precipitation [16]. Zhang et al. (2022) revealed a typical spatial pattern of water conservation in Sanjiangyuan National Park, characterized by "high in the southeast and low in the northwest" [17]. Cao et al. (2020) found that ecological conservation programs significantly enhanced regional water regulation and soil conservation capacity [8]. However, these studies commonly treat permafrost as a static underlying surface condition and rarely incorporate permafrost degradation as an independent driver, resulting in a lack of quantitative assessment of the hydrological effects of permafrost degradation. In contrast, permafrost hydrology generally recognizes that permafrost degradation is not only a surface response to warming but also directly deepens (thickens) the active layer, thereby lowering the aquitard/impermeable layer and altering soil hydraulic properties [7]. Studies on the Qinghai–Tibet Plateau by Gao et al. (2020) [18] and Lv et al. (2022) [19] indicated that ALT deepening alters soil permeability, runoff pathways, and baseflow processes, thereby affecting soil hydraulic properties. A study in the headwaters of the Yellow River by Jin et al. (2022) showed that permafrost degradation has become a key factor shaping groundwater recharge, runoff composition, and changes in vegetation productivity [20]. Yang et al. (2019) reported that permafrost degradation enhances surface–groundwater connectivity and alters regional hydrological cycling processes [21]. However, most of these studies are conducted at site or small catchment scales, and quantitative evaluations of water conservation in permafrost regions at the regional scale remain very limited.

To address the above issues a regional-scale framework was established to quantify ecosystem water conservation and to assess the hydrological influence of permafrost degradation across the TRSR during 1990–2020. Multi-source datasets were integrated, including remote sensing-derived vegetation and land surface characteristics, topographic variables, and gridded climate fields, while permafrost change was represented by active layer thickness (ALT). Water conservation was estimated using the InVEST Water-Yield module (v3.14.2) and interpreted as a proxy of ecosystem water retention/regulation under combined climate–vegetation–surface constraints. The ALT contribution, spatial heterogeneity, and mechanistic pathways were examined using Sen's trend analysis, GeoDetector, geographically weighted regression (GWR), and structural equation modeling (SEM). Nonlinear and delayed responses were further quantified using segmented regression and a distributed lag model (DLM), with robustness evaluated via sensitivity tests to remote sensing inputs.

Specifically, this study aimed to: (1) characterize spatiotemporal changes in water conservation over the past ~30 years and identify the dominant controls; (2) quantify the magnitude, time-lag characteristics, and response thresholds of ALT effects on water conservation; and (3) elucidate mechanisms under the combined influences of climate warming and vegetation change, including differences across watersheds and underlying surface types. The findings support improved understanding of hydrological regulation in alpine permafrost regions and provide scientific evidence for refined water resources management in the TRSR.

2. Materials and Methods

2.1. Study Area and Methods

2.1.1. Study Area

The TRSR is located in the interior of the QTP (31°39′–36°16′N, 89°24′–102°23′E), mainly encompassing the Tibetan autonomous prefectures of Yushu, Golog, Huangnan, and Hainan in Qinghai Province, with a total area of approximately 363,000 km^2 [22] (Figure 1). It is the source area of the Yangtze, Yellow, and Lancang Rivers and is also one of China's key alpine ecological barriers and water conservation zones, known as the "Water Tower of China" [23]. The region has a typical plateau continental climate [24], with a mean annual air temperature of −5.6 to 3.8 °C and mean annual precipitation of 262.2–772.8 mm [25]; spatially it transitions from warm–humid conditions in the southeast to cold–dry conditions in the northwest, with precipitation concentrated mainly in summer and strong evaporation [26]. Controlled by high-elevation topography, vegetation in the study area is dominated by alpine meadow and alpine steppe [27], while swamp meadow and shrub communities develop locally in river valleys and wetlands [28], forming a distinctive alpine wetland–meadow–steppe ecosystem.

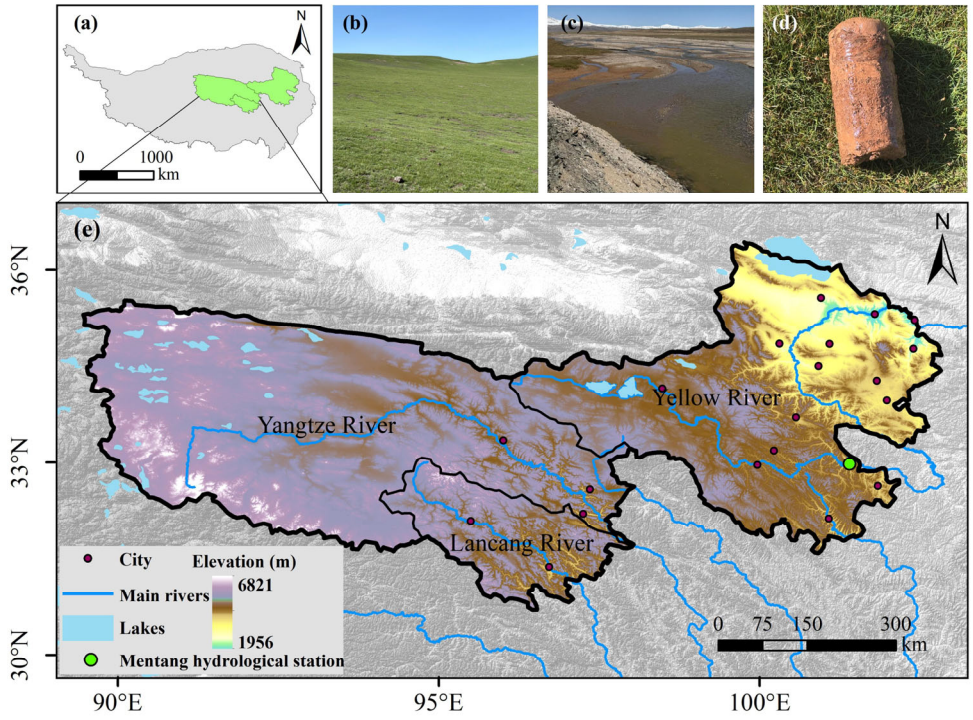

Figure 1. Overview of the TRSR. (**a**) Location of the TRSR on the QTP; (**b**) vegetation landscapes in the TRSR; (**c**) surface rivers in the TRSR; (**d**) ice-rich permafrost; (**e**) topography of the study area and the distribution of major rivers and lakes, main urban settlements, and the Mentang hydrological station.

Permafrost is extensively developed across the TRSR, occurring mainly in high-elevation areas above ~3800–4200 m [29], with a total coverage exceeding 60% [12]. Over recent decades, driven by climate warming and human activities, permafrost has exhibited an accelerated degradation trend, manifested mainly as active layer thickening, ground temperature rising, and ground ice melting [30]; these changes alter ground surface hydrological processes, induce fluctuations in groundwater storage, and intensify soil erosion, thereby exerting profound impacts on water conservation and serving as an important indicator of eco-environmental evolution on the QTP.

2.1.2. Data Sources and Processing

This study used the InVEST model (v3.14.2) to quantify the water conservation capacity in the TRSR of the QTP, and the required inputs mainly included precipitation, evapotranspiration, bedrock depth, soil water parameters, land-use/land-cover types, a biophysical parameter table, DEM, permafrost indicators, and the NDVI [31].

Monthly precipitation at ~1 km resolution was taken from the China gridded monthly precipitation dataset (TPDC: https://data.tpdc.ac.cn/zh-hans/data/faae7605-a0f2-4d18-b28f-5cee413766a2 (accessed on 4 January 2025)) [32] and potential evapotranspiration (PET) from the China gridded monthly PET dataset (~1 km) (TPDC: https://data.tpdc.ac.cn/zh-hans/data/8b11da09-1a40-4014-bd3d-2b86e6dccad4 (accessed on 4 January 2025)) [33]; both datasets cover 1901–2024 at monthly resolution. Land-use/land-cover (LULC) data were obtained from the annual 1 km land-use remote sensing monitoring dataset of China for 1985–2023 (https://gis5g.com/dataResourceDetail?resourcesId=294 (accessed on 4 January 2025)), which was interpreted from Landsat series imagery (MSS, TM, Landsat 7/8/9) via human–machine interactive interpretation and provided through the Geographic Data Sharing Infrastructure, Global Resources Data Cloud [34]. Boundary data were obtained from the National Tibetan Plateau/Third Pole Environment Data Center (TPDC: https://data.tpdc.ac.cn/zh-hans/data/8588327d-f474-4119-b5ab-e599b0f24553 (accessed on 5 January 2025)) [35]. The frozen ground change dataset was also provided by TPDC (https://data.tpdc.ac.cn/zh-hans/data/e03ae441-0af2-4f57-b5b0-0a4f368f4015 (accessed on 5 January 2025)) for 1961–2020 at a 5-year resolution, including permafrost extent, active layer thickness (ALT), and maximum thickness of seasonal frozen ground (MTSFG); permafrost extent is simulated using the TTOP model, and ALT/MTSFG are simulated using the Stefan equation (DOI: 10.11888/Cryos.tpdc.300955) [36]. Bedrock depth was referenced from the bedrock depth map of China (https://www.nature.com/articles/s41597-019-0345-6 (accessed on 5 January 2025)) [37]. Soil water-related parameters were obtained from SoilGrids250m (ISRIC; v2017-03), specifically the derived available soil water capacity until wilting point (WWP; volumetric fraction, v%) provided at seven standard depths; a 0–100 cm (sl1–sl6) thickness-weighted mean was calculated to represent root-zone soil water availability for PAWC parameterization, following Hengl et al. (2017) [38]. Soil texture fractions (sand and clay, %) used for estimating saturated hydraulic conductivity were also obtained from SoilGrids250m (ISRIC; v2017-03) and aggregated to a 0–100 cm (sl1–sl6) thickness-weighted mean before resampling to the common 1 km grid. The biophysical parameter table and runoff coefficients were compiled with reference to studies in comparable regions and the Guidelines for Delineating the Ecological Protection Redline. DEM data were downloaded from the SRTMDEMUTM 90 m product (https://www.gscloud.cn/sources/details/306?pid=302 (accessed on 6 January 2025)) and processed in ArcGIS (ArcMap 10.8) to derive elevation, slope, and aspect. NDVI data were obtained from the AVHRR-CDR reflectance-based product (TPDC: https://data.tpdc.ac.cn/zh-hans/data/f1817320-124b-4633-9309-0f20125e276f (accessed on 6 January 2025)), covering 1982–2020 at a monthly temporal resolution and 0.05° spatial resolution (resampled to 1 km for integrated analyses) [39], and detailed sources are listed in Table 1.

All datasets were categorized into three groups (Table 1): (i) satellite remote sensing products (AVHRR-CDR NDVI, Landsat-based LULC, and SRTM DEM), (ii) reanalysis/model-based outputs (downscaled precipitation, Hargreaves PET, and the frozen ground change product), and (iii) other thematic/vector datasets (bedrock depth, SoilGrids-derived soil parameters, and the study boundary). For each remote sensing product, full metadata (product name, sensor/platform, version/collection, spatial/temporal resolution, processing level, and access link/DOI) are provided in Table 1.

Table 1. Data sources and processing.

Data Category	Dataset	Key Metadata	Spatial and Temporal Resolution	Access Link/DOI
Reanalysis/ model outputs	China 1 km gridded monthly precipitation dataset	Delta downscaling based on the CRU 0.5° climate dataset and WorldClim high-resolution climatology	1 km; monthly; 1901–2024	https://data.tpdc.ac.cn/zh-hans/data/faae7605-a0f2-4d18-b28f-5cee413766a2 (accessed on 4 January 2025); https://doi.org/10.12041/geodata.192891852410344.ver1.db
Reanalysis/ model outputs	China 1 km monthly potential evapotranspiration dataset	PET computed from the China 1 km monthly mean/min/max temperature dataset using the Hargreaves method	1 km; monthly; 1901–2024	https://data.tpdc.ac.cn/zh-hans/data/8b11da09-1a40-4014-bd3d-2b86e6dccad4 (accessed on 4 January 2025); https://doi.org/10.11866/db.loess.2021.001
Remote sensing products	Annual 1 km land-use/land-cover (LULC) remote sensing monitoring dataset of China	Land-cover classification product interpreted from Landsat series imagery (MSS, TM, and Landsat 7/8/9) via human–machine interactive interpretation (product type: Landsat-based classification); 6 Level-1 and 25 Level-2 classes; resampled to 1 km for this study	1 km; annual; 1985–2023	https://gis5g.com/dataResourceDetail?resourcesId=294 (accessed on 4 January 2025)
Remote sensing products	SRTMDEMUTM 90 m digital elevation model product	SRTM-based DEM (SRTM3 v4.1)	90 m (static)	https://www.gscloud.cn/sources/details/306?pid=302 (accessed on 4 January 2025)
Other gridded/ vector datasets	Study region boundary (TRSR)	Vector boundary for masking/clipping	static	https://data.tpdc.ac.cn/zh-hans/data/8588327d-f474-4119-b5ab-e599b0f24553 (accessed on 4 January 2025); https://doi.org/10.11888/Geogra.tpdc.270009
Reanalysis/ model outputs	Qinghai–Tibet Plateau permafrost change dataset	Remote sensing land surface temperature and meteorological stations; permafrost extent simulated by the TTOP model; ALT simulated by the Stefan equation	1 km; 5 year; 1961–2020	https://data.tpdc.ac.cn/zh-hans/data/e03ae441-0af2-4f57-b5b0-0a4f368f4015 (accessed on 4 January 2025); https://doi.org/10.11888/Cryos.tpdc.300955

Table 1. *Cont.*

Data Category	Dataset	Key Metadata	Spatial and Temporal Resolution	Access Link/DOI
Thematic datasets	Bedrock depth data	Thematic bedrock depth product	Native resolution per dataset documentation (static)	https://www.nature.com/articles/s41597-019-0345-6 (accessed on 4 January 2025); https://doi.org/10.6084/m9.figshare.11358929
Thematic datasets	SoilGrids250m soil properties	WWP (v%), sand/clay (%), 7 depth layers; 0–100 cm (sl1–sl6) thickness-weighted mean; Ks derived via pedotransfer	v2017-03; 250 m (static)	https://docs.isric.org/globaldata/soilgrids/SoilGrids_faqs_2017.html (accessed on 4 January 2025); https://doi.org/10.1371/journal.pone.0169748
Remote sensing products	Normalized difference vegetation index (NDVI)	Derived from the 0.05° AVHRR-CDR surface reflectance product (red/NIR bands)	1 km, monthly; 1982–2020	https://data.tpdc.ac.cn/zh-hans/data/f1817320-124b-4633-9309-0f20125e276f (accessed on 4 January 2025); https://doi.org/10.11888/Terre.tpdc.300473

Spatially, all datasets were resampled to a 1 km × 1 km resolution and projected in WGS 1984. Continuous variables (e.g., climate, NDVI, and ALT) were resampled using bilinear interpolation, whereas categorical variables (e.g., LULC and permafrost types) were resampled using nearest-neighbor resampling to preserve class codes and avoid class mixing and spurious categories induced by interpolation. Temporally, the study period was 1990–2020; climate variables were aggregated to annual means or totals, and the NDVI was averaged over the growing season (June–September) each year. To ensure temporal consistency, ALT data were primarily taken from the 5-year-resolution dataset (China permafrost active layer thickness dataset, 1961–2020) and converted into an annual series using linear interpolation. The interpolation performance was evaluated using leave-one-out cross-validation, yielding a mean error of <0.05 m. For subsequent statistical and lag analyses (e.g., GeoDetector/GWR/SEM), variables were detrended and standardized (z-score) to reduce spurious correlations caused by shared trends; the InVEST simulations used the original (non-standardized) variables in physical units.

The AVHRR-CDR reflectance-based NDVI product has been reported to agree well with MODIS vegetation products over the Tibetan Plateau (RMSE = 0.0545; r = 0.926), supporting its suitability for long-term vegetation dynamics analysis in this region and period [40]. The SRTM3 v4.1 DEM has been evaluated over the Tibetan Plateau against DGPS points and a topographic map-derived DEM, indicating its suitability for regional terrain characterization [41]. Landsat time-series land-cover products for China have reported an overall accuracy of 79.31% based on large visually interpreted sample sets, supporting the use of Landsat-derived LULC for regional-scale parameterization [42].

According to the parameter requirements of the InVEST Annual Water-Yield Model, corresponding biophysical parameters must be specified for different LULC types. After consistently reclassifying the LULC data for the TRSR, the biophysical parameter table used in the model (Table 2) was constructed by referring to the official InVEST documentation and related studies, including LULC_veg, rooting depth (root_depth), and the

crop coefficient (Kc). In Table 2, LULC_veg is a code indicating whether a given LULC class is vegetated, enabling the model to distinguish vegetated from non-vegetated pixels when calculating AET and to call vegetation-related parameters accordingly. All vegetated classes were assigned a value of 1 and all other classes a value of 0. The model uses the biophysical table to assign rooting depth and Kc to each LULC class, thereby mapping LULC to biophysical parameters in space and supporting subsequent gridded simulations of water yield and water conservation.

Table 2. Biophysical parameter table for the InVEST Water-Yield Model.

Land-Use Type	LULC_veg	Crop Coefficient (Kc)	Rooting Depth (mm)
Cropland	1	0.70	300
Forest	1	1.00	3000
Grassland	1	0.65	250
Water bodies	0	0.90	1
Built-up land	0	0.30	1
Unused land	0	0.50	100

2.2. Methods

2.2.1. Assessment of Water Conservation Capacity

Water conservation capacity is operationally quantified as a pixel-level water conservation indicator (mm) derived from the InVEST (v3.14.2) annual water yield output. Annual water yield (mm) represents the portion of precipitation not consumed by actual evapotranspiration and thus provides the hydrological basis for estimating ecosystem-regulated water retention, while the derived water conservation indicator further incorporates terrain and soil hydraulic constraints to capture spatial heterogeneity in retention and flow regulation. All required inputs and their sources/resolutions are summarized in Table 1, and the selection and justification of the Zhang coefficient Z are provided in Section 2.2.7.

The InVEST model is a suite of tools for assessing ecosystem services, and its Water-Yield Model is a sub-module used to estimate water yield generated within a region as a result of precipitation and evapotranspiration processes. The model is primarily based on the Budyko hydrothermal coupled balance hypothesis and derives grid-based water yield from the imbalance between precipitation and actual evapotranspiration (AET) [34], as expressed by the following equation(s):

$$Y_x = \left(1 - \frac{AET_x}{P_x}\right) \times P_x \tag{1}$$

In the equation, Y_x denotes annual water yield (mm), while AET_x and P_x represent the annual actual evapotranspiration and annual precipitation (mm) of pixel x, respectively. $\frac{AET_x}{P_x}$ represents an approximation of the Budyko curve and is computed using the Budyko curve formulation proposed by Fu et al. (1981) [43]:

$$\frac{AET_x}{P_x} = 1 + \frac{PET_x}{P_x} - \left[1 + \left(\frac{PET_x}{P_x}\right)^{\omega_x}\right]^{\frac{1}{\omega_x}} \tag{2}$$

In this expression, PET_x denotes the PET (mm) for pixel x, and ω_x is an empirical (non-physical) calibration parameter representing catchment climate conditions and soil attributes. The parameter is computed using the following equation:

$$\omega_x = Z\frac{AWC_x}{P_x} + 1.25 \tag{3}$$

In the equation, Z denotes the Zhang coefficient, which captures regional rainfall regime and hydrological behavior (typically 1–30); AWC_x represents plant available water content (mm) as a function of soil texture and soil depth, computed as:

$$AWC_x = \min(MRBD, \mathrm{SD}) \times PAWC \quad (4)$$

MRBD is the root restricting layer depth (mm), *SD* denotes soil depth (mm), and *PAWC* represents plant available water content, defined as the difference between field capacity and the permanent wilting point. PAWC was derived from SoilGrids250m (ISRIC; v2017-03) using the soil water metric (WWP; volumetric fraction, v%). Values were aggregated to a 0–100 cm profile (sl1–sl6) using a thickness-weighted mean to represent root-zone water availability.

Based on the estimated water yield, grid-scale water conservation was calculated by integrating the topographic index, surface flow velocity coefficient, and soil saturated hydraulic conductivity in the study area as follows:

$$WC_i = min\left(1, \frac{249}{V}\right) \times min\left(1, \frac{0.9 \times TI}{3}\right) \times min\left(1, \frac{K_s}{300}\right) \times Y_i \quad (5)$$

$$TI = lg\frac{D_{area}}{Soil\ depth \times P_{slope}} \quad (6)$$

$$K_s = 60.96 \times 10^{(-0.6+0.0126S-0.0064C)} \quad (7)$$

In this equation, WC_i denotes pixel-level water conservation (mm), and Yi denotes water yield (mm); TI is the topographic index, Ks is saturated hydraulic conductivity (mm d^{-1}), D_{area} is soil layer depth (mm), $Soil_{dep}$ is soil depth (mm), P_{slope} is slope gradient expressed as a percentage (%), and S and C are the sand and clay fractions (%) obtained from SoilGrids250m (ISRIC; v2017-03) and aggregated to a 0–100 cm (sl1–sl6) thickness-weighted mean.

2.2.2. Robustness Check for Permafrost Effects Under ALT Uncertainty

A targeted sensitivity test was conducted to evaluate whether the inferred permafrost effects are robust to uncertainty in ALT. Based on the leave-one-out cross-validation error of the annualized ALT series (Section 2.1.2), a plausible uncertainty range of ±0.05 m was adopted. Because GeoDetector requires discretized strata, this perturbation was implemented by shifting the ALT strata upward and downward by one class, followed by re-estimation of the q-statistics. The resulting ranges of q values are reported in Table S1 and are used to assess the robustness of the main inferences under ALT uncertainty.

2.2.3. Trend in Permafrost Degradation

This study used the QTP permafrost change dataset (1990–2020), which mainly includes gridded mean annual ALT and permafrost-type classification data. The dataset was first masked using the TRSR vector boundary to standardize spatial coverage, all variables were resampled to 1 km resolution using bilinear interpolation, and missing ALT values were filled by linear interpolation in the time domain [44]. To quantify permafrost degradation trends, Sen's slope estimator (Theil–Sen median) was applied to the pixel-wise ALT time series, as follows:

$$\theta_{sen} = median\left(\frac{ALT_j - ALT_i}{t_j - t_i}\right), \forall t_j > t_i \quad (8)$$

In the equation, θ_{sen} represents the Sen's slope (Theil–Sen estimator), i.e., the median of all pairwise slopes of ALT over time. ALT_i and ALT_j denote the ALT at times t_i and t_j (years), respectively. The unit of θ_{sen} is mm a^{-1}. A positive θ_{sen} indicates an increasing ALT trend, whereas a negative value indicates a decreasing trend.

2.2.4. Analysis of Factors Influencing Water Conservation Capacity

In this study, the GeoDetector model was used to analyze the effects of different environmental factors (potential evapotranspiration (PET), precipitation (PPT), ALT, elevation, and vegetation condition (NDVI)) on the spatial differentiation of water conservation [45]. The key metric is the q statistic:

$$q = 1 - \frac{\sum_{h=1}^{L} N_h \sigma_h^2}{N\sigma^2} \tag{9}$$

In this formulation, $q \in [0, 1]$, with higher values indicating greater explanatory strength; N_h and ${\sigma_h}^2$ denote the number of samples and the variance in stratum h, whereas N and σ^2 represent the total sample size and overall variance. Continuous predictors were discretized into strata using Jenks Natural Breaks, and statistical significance was evaluated via 999 permutations.

To characterize spatial non-stationarity in the ALT–water conservation relationship, GWR was employed [46]:

$$WC_i = \beta_0(u_i, v_i) + \sum_{k=1}^{p} \beta_k(u_i, v_i) \times X_{ik} + \varepsilon_i \tag{10}$$

In this model, $\beta_0(u_i, v_i)$ is the location-specific intercept at (u_i, v_i), $\beta_k(u_i, v_i)$ is the local coefficient for predictor X_{ik}, and ε_i is the residual error. Here, WC_i denotes water conservation at location i, and the predictors X_k include ALT, precipitation, DEM, NDVI, and PET. Bandwidth selection was based on the corrected Akaike information criterion (AICc), using a search procedure to identify the bandwidth that minimized AICc, and a Gaussian kernel was used for weighting. To improve regression stability and make coefficients comparable across predictors with different scales, all continuous candidate predictors (ALT, precipitation, DEM, NDVI, and PET) were standardized prior to model fitting by centering on the global mean and scaling by the SD, yielding dimensionless variables with mean = 0 and SD = 1. To diagnose multicollinearity, VIFs were computed for the predictors, and observations associated with VIF > 10 were treated as abnormal and removed from the GWR fitting to avoid unstable local estimates. After model fitting, spatial autocorrelation in GWR residuals was evaluated using Moran's I; residuals were considered spatially independent when $p > 0.05$, indicating no significant spatial dependence.

2.2.5. Identification of Critical Points and Lag Effects

To detect the potential critical thresholds in the impact of permafrost degradation on water conservation, a piecewise linear regression model was employed [47]:

$$WC = \begin{cases} a_1 + b_1 \times ALT, ALT < c \\ a_2 + b_2 \times ALT, ALT \geq c \end{cases} \tag{11}$$

In this model, c denotes the breakpoint. Confidence intervals were derived via bootstrapping (1000 iterations). Given the limited explanatory power, the breakpoint was treated only as an indicative threshold for identifying potentially sensitive zones, rather than a definitive threshold.

To incorporate lagged responses of water conservation to permafrost change, distributed lag model (DLM) was built [48]:

$$WC_t = \alpha + \sum_{k=0}^{K} \beta_k \, ALT_{t-k} + \gamma X_t + \varepsilon_t \quad (12)$$

In this framework, K is the maximum lag length (10 years in this study), X_t represents the control covariates (precipitation, temperature, and NDVI), and β_k is the coefficient associated with the k-year lag. To mitigate multicollinearity and prevent overfitting, ridge-regression regularization was applied. Statistical significance of lag coefficients was assessed using a bootstrap permutation procedure with 1000 resamples.

2.2.6. SEM for Environmental Effects on the Water Conservation Function

To disentangle the direct and indirect pathways through which permafrost degradation affects water conservation, SEM was constructed in Python (version 3.13). SEM allows multiple causal relationships to be examined within a single framework and enables quantitative separation of direct versus indirect effects on the response variable, and it is widely applied to elucidate processes in complex ecohydrological systems. Guided by hydrological characteristics of permafrost regions, ALT, precipitation, evapotranspiration, vegetation-cover index, and elevation were treated as exogenous variables, with water conservation specified as the endogenous variable, to define a set of hypothesized causal paths. Before SEM fitting, all variables were normalized and detrended to eliminate scale effects and shared temporal trends. SEM parameters were estimated using the Python library semopy, and path coefficients were obtained using MLE; model fit was evaluated using χ^2, CFI (Comparative Fit Index), RMSEA (Root Mean Square Error of Approximation), and related metrics. Path visualization was implemented using graphviz and the built-in plotting utilities of semopy.

2.2.7. InVEST Model Calibration and Performance Evaluation

To evaluate the suitability and accuracy of the InVEST Water-Yield Module for runoff simulation in the study region, the annual mean discharge record YIE (1990–2016) from the Mentang hydrological station on the main channel of the Yellow River headwaters was used to calibrate the key parameter Z (Zhang coefficient) and to evaluate model performance. The catchment monitored at Mentang station is located in the permafrost seasonally frozen ground transition zone, where seasonally frozen ground prevails along the main river valley but patchy permafrost remains in high mountains and the upper portions of certain tributaries; consequently, runoff dynamics integrate hydrological signals from continuous and discontinuous permafrost as well as seasonally frozen ground, allowing for regional scale constraints on water budget simulations in the TRSR. For calibration, the upstream contributing area of the Mentang station was delineated in Google Earth Engine (GEE) using an existing DEM layer as a computational/GIS workflow rather than for remote sensing product generation or preprocessing. Model-derived annual water yield was then aggregated across the delineated catchment using area-weighted averaging to generate a station comparable annual simulated mean discharge time series. The Zhang parameter (Z) was iteratively tuned within the plausible range (Z = 1–30), and agreement between simulated and observed annual mean discharge was evaluated in terms of both interannual variability and absolute magnitude; the Z value that minimized the overall error and maximized correlation was selected as optimal. Model performance was assessed using the R^2, correlation coefficient (r), RMSE, NSE, PBIAS, and related indices.

3. Results

3.1. Parameter Selection

During model calibration, the Z parameter was adjusted, and agreement between simulated and observed annual mean discharge was evaluated in terms of both inter-annual variability and absolute magnitude. The runoff time series (Figure 2a) shows that when Z was set to 3.5, simulated and observed runoff exhibited consistent inter-annual trends and similar fluctuations over 1990–2016. The scatter plot (Figure 2b) indicates that the fitted relationship is close to the 1:1 line, suggesting that the model reproduces observed runoff reasonably well at Z = 3.5.

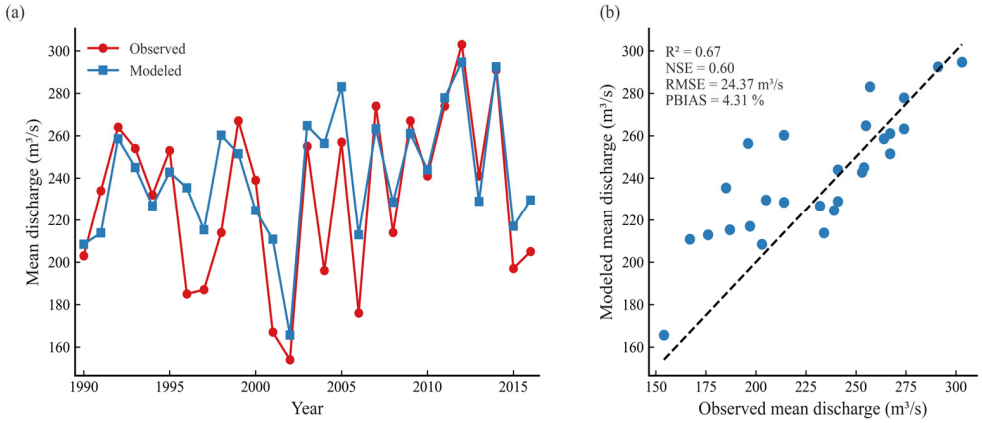

Figure 2. Model calibration and performance evaluation for InVEST runoff simulation. (**a**) Comparison of observed and simulated annual mean discharge for 1990–2016; (**b**) scatter plot of observed versus simulated annual runoff and the fitted relationship.

Model performance was quantified using multiple metrics. In addition, the Nash–Sutcliffe efficiency (NSE) and percent bias (PBIAS) were also computed (Figure 2b). The root mean square error (RMSE) was 24.37 m^3 s^{-1}, and the relative RMSE was 4.31%, indicating a low average deviation between simulated and observed values. The coefficient of determination (R^2) was 0.67 and the correlation coefficient (r) was 0.82, both indicating a strong linear association between simulated and observed runoff.

3.2. Spatiotemporal Patterns of Water Conservation

3.2.1. Spatial Distribution of Water Conservation

Based on InVEST simulations for 1990–2020, water conservation in the TRSR shows pronounced spatial heterogeneity, with an overall pattern of gradually decreasing values from the southeast to the northwest (Figure 3a). These spatial differences are jointly influenced by regional climatic gradients, topographic relief, vegetation types, and permafrost conditions.

The humid southeastern zone is strongly influenced by the southwest monsoon, with mean annual precipitation reaching 500–700 mm. Favorable hydrothermal conditions support alpine meadows and alpine marshes with high-cover and well-developed root systems, as well as soils with relatively high porosity and moisture content, resulting in strong precipitation interception and storage and generally high water conservation of 200–300 mm. Actual evapotranspiration in this zone reaches 900–1000 mm (Figure 3c), indicating an active water cycle; nevertheless, abundant precipitation and strong soil water-holding capacity maintain relatively high levels of water conservation. In contrast, the arid northwestern zone receives only 200–300 mm of mean annual precipitation and has a cold–dry climate with relatively high evapotranspiration (~300–500 mm; Figure 3c); vegetation is dominated by alpine steppe and desert steppe with sparse cover, and soils are relatively

sandy with rapid infiltration and poor water retention, leading to rapid loss of surface moisture and water conservation generally below 100 mm (Figure 3a). Annual water yield in this area is mostly <200 mm (Figure 3b), indicating limited capacity to support downstream runoff. Meanwhile, ALT is relatively large (up to 2.5–3.5 m; Figure 3d), and the deeper permafrost table promotes downward percolation of soil water, limiting moisture storage in shallow soils and further weakening water conservation capacity.

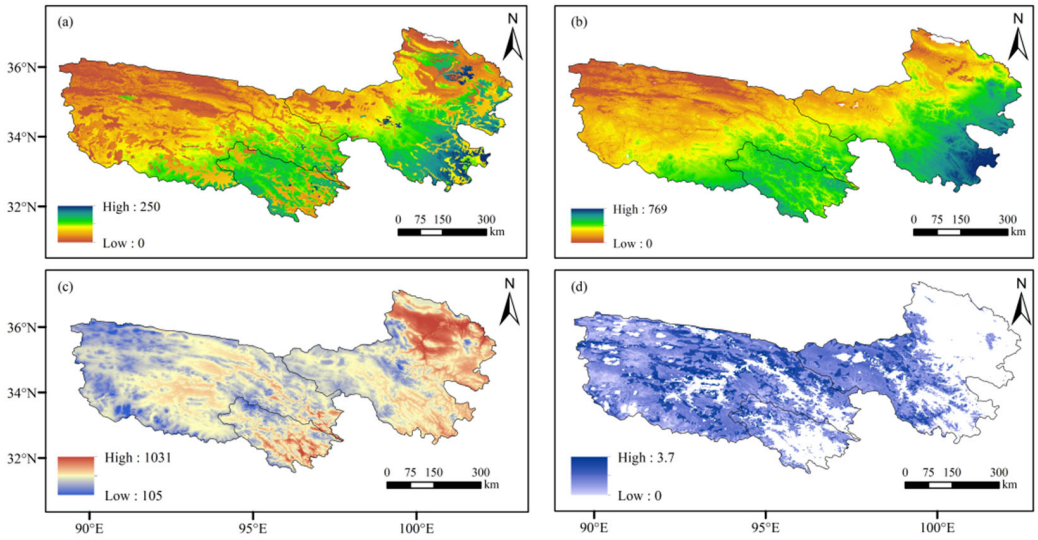

Figure 3. Spatial patterns of the hydro-environmental variables in the TRSR. (**a**) Water conservation (mm); (**b**) water yield (mm); (**c**) actual evapotranspiration (mm); (**d**) ALT (m).

3.2.2. Temporal Evolution of Water Conservation

From 1990 to 2020, water conservation capacity in the TRSR exhibited a fluctuating upward trend, with a rate of increase of 0.64 mm a^{-1} (Figure 4). In the Yellow River headwaters, water conservation capacity increased from 45 mm in 1990 to 65 mm in 2020 (44% increase). In the Yangtze River headwaters, water conservation capacity increased from 25 mm in 1990 to 38 mm in 2020 (52% increase); values were relatively low in 1994 and 2004, whereas water conservation capacity exceeded 40 mm in both 2006 and 2012. By comparison, the Lancang River headwaters exhibited the highest baseline and the strongest variability: water conservation capacity was 63 mm in 1990, increased to 72 mm in 2020 (14% increase), and exceeded 80 mm in 1994, 2010, and 2016. Regionally, 1994 marked the lowest water conservation capacity in the TRSR: relative to 1992, capacity in the Yellow, Yangtze, and Lancang headwaters decreased by 15, 8, and 25 mm, respectively. This reduction coincided with 20–30% below-normal precipitation and 1–2 °C above-normal temperature during 1993–1994; drought likely enhanced vegetation transpiration and exacerbated soil moisture deficits, and—together with ALT thickening—collectively reduced regional water conservation capacity. In 2006, water conservation capacity peaked in the Yellow and Lancang headwaters and increased markedly in the Yangtze headwaters, coincident with a significant increase in the NDVI and ~15% above-normal precipitation. In 2012, water conservation capacity in the Lancang headwaters increased markedly (>80 mm), which is associated with higher precipitation and a longer ALT thaw period, allowing more water to be retained.

Moreover, stage-wise analysis indicates that water conservation capacity remained relatively low and increased slowly during 1990–2000, rose more rapidly during 2000–2010, and then stayed at a higher level with minor fluctuations after 2010.

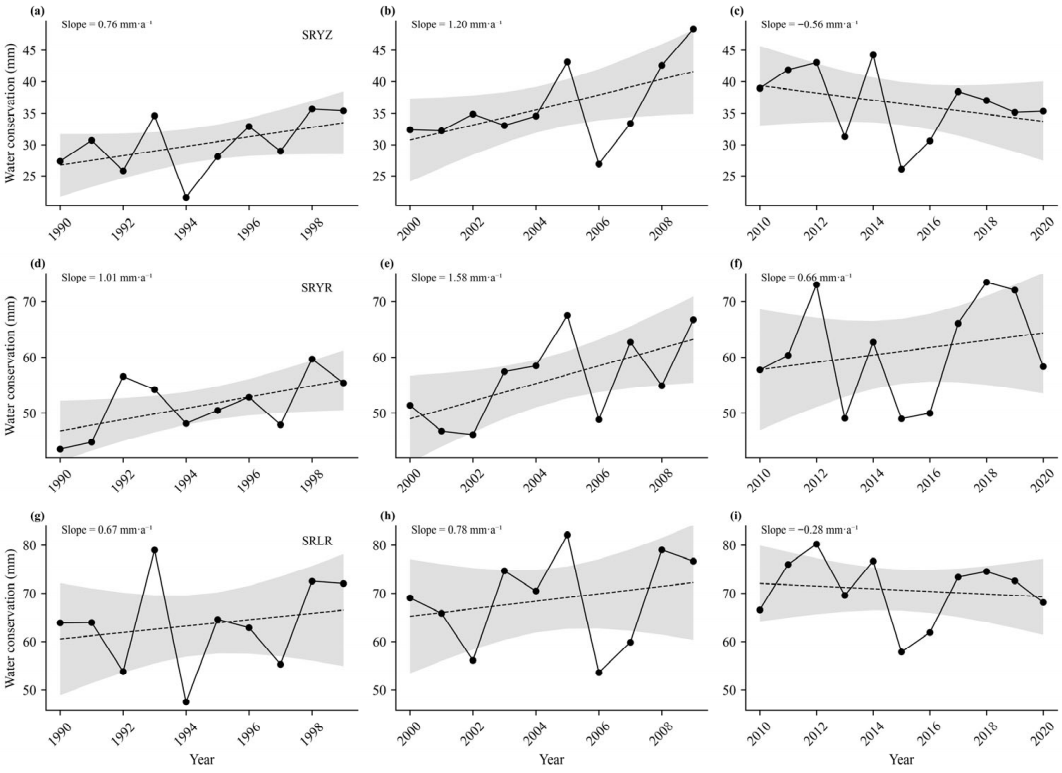

Figure 4. Temporal evolution of water conservation in the TRSR. Panels (**a**–**c**) shows the Yangtze River source area (SRYZ), (**d**–**f**) the Yellow River source area (SRYR), and (**g**–**i**) the Lancang River source area (SRLR); the three columns correspond to 1990–1999, 2000–2009, and 2010–2020, respectively. The dotted lines indicate the fitted linear trends, and the gray shaded areas represent the 95% confidence intervals.

3.3. Coupled Trends in ALT and Water Conservation in Permafrost Areas

Using multi-source remote sensing and model-simulated data, a coupling analysis was conducted to examine the spatiotemporal patterns of ALT and water conservation in the TRSR. Spatially, the change rate of water conservation (Figure 5a) shows pronounced regional correspondence with the change rate of ALT (Figure 5b). Areas of increasing water conservation largely overlap with ALT-thickening zones in the central-southern Yangtze headwaters and parts of the Lancang headwaters, whereas areas of decreasing water conservation coincide with ALT-thinning zones in the northern Yellow River headwaters and some localized areas in the western Yangtze headwaters. Statistically, ~92% of permafrost areas exhibit consistent trends between ALT and water conservation, indicating coordinated spatiotemporal evolution between the two variables. Temporally, ALT increased significantly during 1990–2020 (Sen's slope = 0.32 cm a^{-1}, $p < 0.05$), while water conservation increased concurrently with inter-annual fluctuations (Sen's slope = 1.23 mm a^{-1}, $p < 0.05$). However, during certain sub-periods (e.g., 2000–2005), accelerated ALT thickening (0.45 cm a^{-1}) was accompanied by a temporary stagnation in the increase of water conservation (slope = 0.21 mm a^{-1}), implying lag effects and potential threshold behavior in the influence of permafrost degradation on water conservation. Further analysis of the relationship between the ALT change slope and the water conservation change slope shows a weak positive correlation (r = 0.38, $p < 0.05$), suggesting that ALT thickening is associated with increased water conservation in most areas.

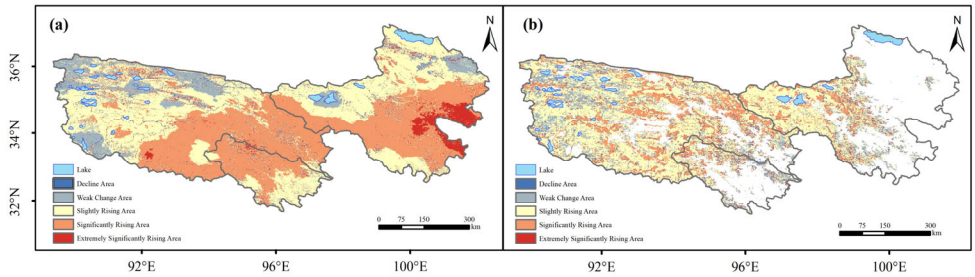

Figure 5. Coupled analysis of trend changes in water conservation and ALT in the TRSR. (**a**) Changes in water conservation; (**b**) changes in ALT.

4. Discussion

4.1. Drivers of the Water Conservation Function in the TRSR

GeoDetector results quantifying spatial heterogeneity and factor interactions (Table 3) show that precipitation has the strongest explanatory power for the water conservation function (q = 0.704, $p < 0.05$), indicating that the spatial pattern of water conservation function in this region is primarily dominated by precipitation. The NDVI (q = 0.177) and DEM (q = 0.088) ranked next, reflecting the ecohydrological roles of vegetation in precipitation interception and topography in modulating runoff. The single-factor explanatory power of ALT (q = 0.024) was relatively low, comparable to that of PET (q = 0.023). The robustness test under ±0.05 m ALT uncertainty yields q values ranging from 0.010 to 0.019 (Table S1), indicating that the qualitative conclusion regarding the comparatively weak direct explanatory power of ALT remains unchanged. Multi-factor interaction results (Table 4) further show that synergistic effects between precipitation and other factors substantially enhance the explanatory power for the water conservation function. The interaction q value between precipitation and ALT was 0.736, representing a 4.5% increase relative to precipitation alone; interaction q values between precipitation and the NDVI as well as precipitation and DEM were also higher than the corresponding single-factor levels. In addition, interaction q values between ALT and the NDVI (q = 0.224) and between ALT and DEM (q = 0.157) suggest that permafrost influences on the water conservation function depend partly on vegetation and topographic conditions; in high-elevation areas with a high NDVI, the effects of ALT changes on the water conservation function are more complex.

Table 3. Factor detection results from GeoDetector.

	PET	PPT	ALT	Elevation	NDVI
q value	0.023	0.704	0.024	0.088	0.177

Note: PET: potential evapotranspiration; PPT: precipitation; ALT: active layer thickness; NDVI: normalized difference vegetation index.

Table 4. Interaction detection results from GeoDetector.

	PET	PPT	ALT	Elevation	NDVI
PET	0.023				
PPT	0.772	0.704			
ALT	0.079	0.736	0.024		
Elevation	0.140	0.735	0.157	0.088	
NDVI	0.207	0.738	0.224	0.221	0.177

Note: PET: potential evapotranspiration; PPT: precipitation; ALT: active layer thickness; NDVI: normalized difference vegetation index.

The SEM results (Figure 6) further support an overall pathway of "climate dominance and land surface modulation". Precipitation exerts the strongest positive effect on the water

conservation function ($\beta = 0.86$, $p < 0.001$), whereas elevation shows a significant negative effect ($\beta = -0.10$, $p < 0.001$). ALT is significantly and positively associated with the water conservation function ($\beta = 0.03$, $p = 0.022$), suggesting that active layer deepening may increase soil water storage space and enhance groundwater recharge and ecohydrological buffering to some extent. PET has a significant negative effect on the water conservation function ($\beta = -0.12$, $p < 0.001$). In contrast, the NDVI positively affects PET ($\beta = 0.05$, $p = 0.007$) and shows a slightly negative but non-significant effect on ALT ($p > 0.05$).

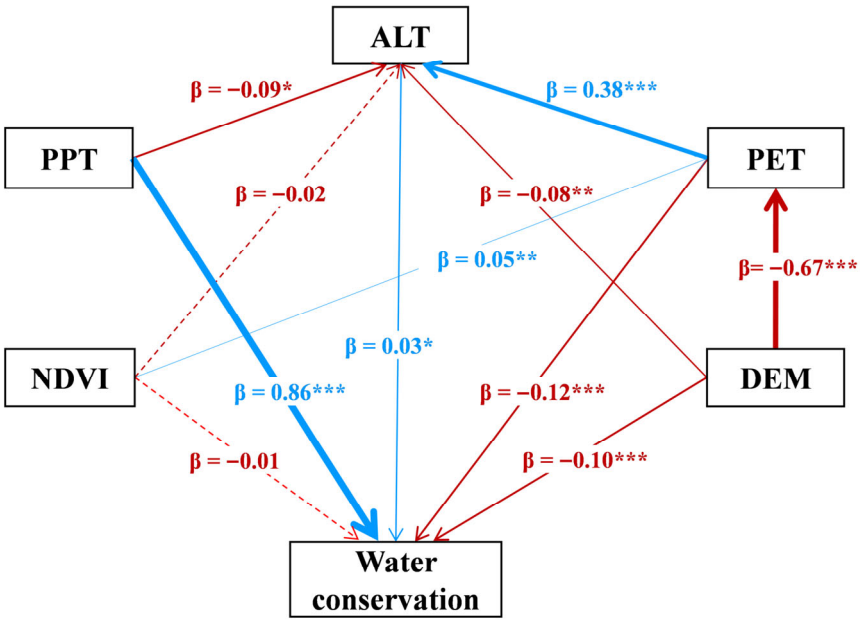

Figure 6. Path analysis of environmental factors influencing water conservation in the TRSR. Solid lines represent statistically significant paths ($p \leq 0.05$), while dashed lines indicate nonsignificant paths. Bluearrows denote positive effects, and red arrows indicate negative effects. The standardized path coefficients (β) and significance levels are displayed along each arrow. (PPT: precipitation; NDVI: normalized difference vegetation index; ALT: active layer thickness; PET: potential evapotranspiration; DEM: digital elevation model). Note: * $p < 0.05$, ** $p < 0.01$, *** $p < 0.001$.

These results co-confirm that precipitation is the primary control on the spatial heterogeneity and inter-annual variability of the water conservation function, consistent with previous studies on hydrological processes in the TRSR and the QTP, which indicate that precipitation change has been one of the main drivers of recent variations in regional runoff and water supply [10,49]. By controlling ecosystem water inputs, precipitation directly determines the baseline levels of water yield and water conservation in InVEST. Areas with a high NDVI generally exhibited a stronger water conservation function, reflecting the roles of canopy interception, litter layer cover, and root development in enhancing soil water storage and regulating surface runoff [50]. Numerous studies based on watershed observations and hillslope experiments have shown that vegetation restoration can significantly increase soil infiltration and soil moisture, attenuate storm runoff, and thereby enhance water conservation capacity [51,52]. Topographic factors also constrain the water conservation function by regulating moisture transport, spatial precipitation patterns, and hillslope runoff generation–concentration pathways. Although permafrost alone shows a relatively weak effect on the water conservation function, changes in ALT can alter soil hydraulic conductivity and pore connectivity, thereby controlling the partitioning of precipitation among surface runoff, shallow storage, and deep drainage [13,53]. In addition, the results suggest that vegetation and permafrost jointly regulate soil water storage and evapotranspiration processes. In areas with high vegetation cover, dense organic matter and roots

can enhance soil aggregate stability and water-holding capacity, thereby amplifying the "increased storage space" effect induced by ALT deepening [54]. In degraded grasslands or sparse steppe, freeze–thaw disturbance more readily disrupts soil structure and promotes rapid water leakage/percolation [50].

Within permafrost areas, multivariate GWR was further used to characterize local responses of the water conservation function to permafrost, climate, and underlying surface factors (Figure 7). Overall, the regression coefficients (β) exhibit pronounced spatial variability, indicating strong spatial differences in the controls of the water conservation function. Specifically, β for ALT (Figure 7a) is predominantly positive in the Yangtze and Lancang headwaters, whereas negative values are relatively concentrated in the Yellow headwaters. Precipitation (Figure 7b) shows mainly positive effects, with larger positive coefficients in the Yangtze headwaters. β for DEM (Figure 7c) differs markedly among headwater regions, with contrasting signs between some high-elevation mountain areas and low-lying river valleys. The NDVI (Figure 7d) is positive overall, but negative coefficients occur in some localized areas. PET (Figure 7e) is predominantly negative. Overall R^2 values (Figure 7f) are moderate to high, reaching higher levels in parts of the Yangtze and Yellow headwaters, whereas low-R^2 areas are more evident in the eastern portion.

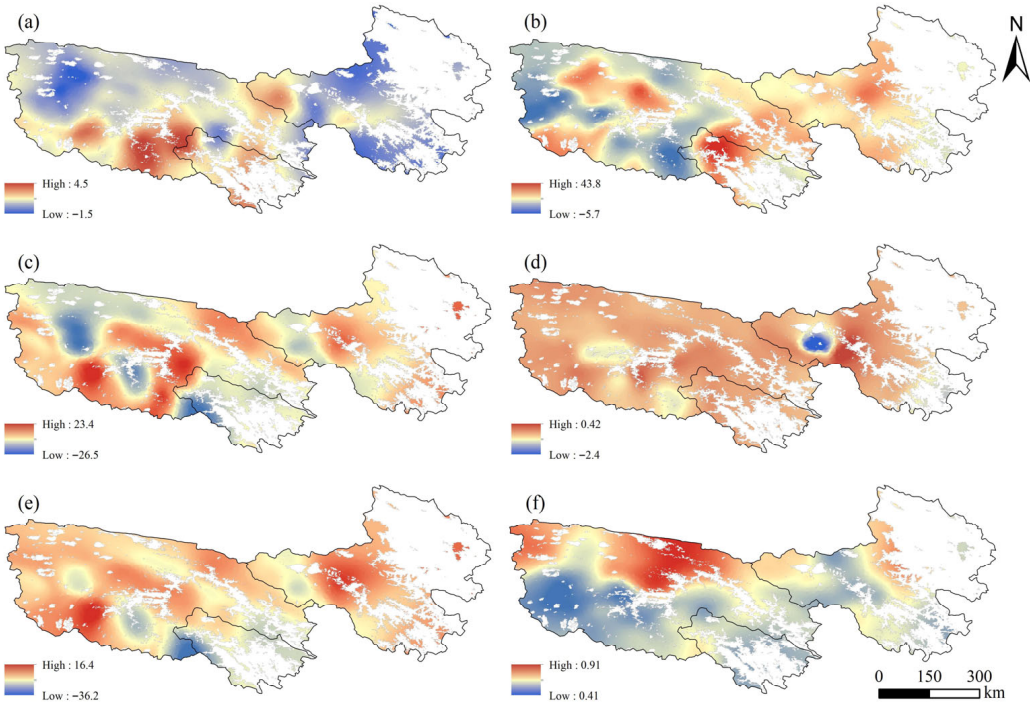

Figure 7. Independent effects of different driving factors on the water conservation function in permafrost areas of the TRSR. (**a**) ALT; (**b**) precipitation; (**c**) DEM; (**d**) NDVI; (**e**) PET; (**f**) local R^2.

These results indicate pronounced spatial non-stationarity in the effects of different factors on the water conservation function. In semi-humid zones, regression coefficients for precipitation and the NDVI are generally larger, suggesting that the water conservation function is jointly controlled by water inputs and vegetation condition. In areas with concentrated permafrost distribution and high ground-ice content, the regression coefficient of ALT increases markedly and, in some locations, even exceeds those of precipitation and the NDVI, indicating a "permafrost-dominated" hydrological regime. This pattern is consistent with diagnostic findings on permafrost degradation and runoff changes in the Yangtze and Yellow headwaters [55,56].

4.2. Mechanisms of Permafrost Degradation Effects on the Water Conservation Function

A segmented linear relationship exists between ALT and water conservation in the TRSR (Figure 8), with a clear breakpoint at ALT ≈ 1.77 m (95% CI: 1.73–2.46 m), indicating a potential sensitivity threshold. Segmented regression was adopted to provide an interpretable breakpoint estimate and two-sided slopes with uncertainty (bootstrap 1000 iterations), facilitating a quantitative threshold description rather than relying on a single global correlation metric. Below this threshold, water conservation increases slightly with increasing ALT (slope = +23.18 mm m^{-1}), likely related to shallow thaw–freeze processes that enhance infiltration and seasonal water redistribution during freeze–thaw cycles. However, once ALT exceeds the threshold, water conservation begins to decline (slope = −0.53 mm m^{-1}), indicating reduced near-surface water retention and potentially enhanced leakage/percolation losses as thaw deepens. This threshold implies that as the ALT deepens, the ecohydrological system may shift from a storage-dominated state to one dominated by leakage/percolation losses.

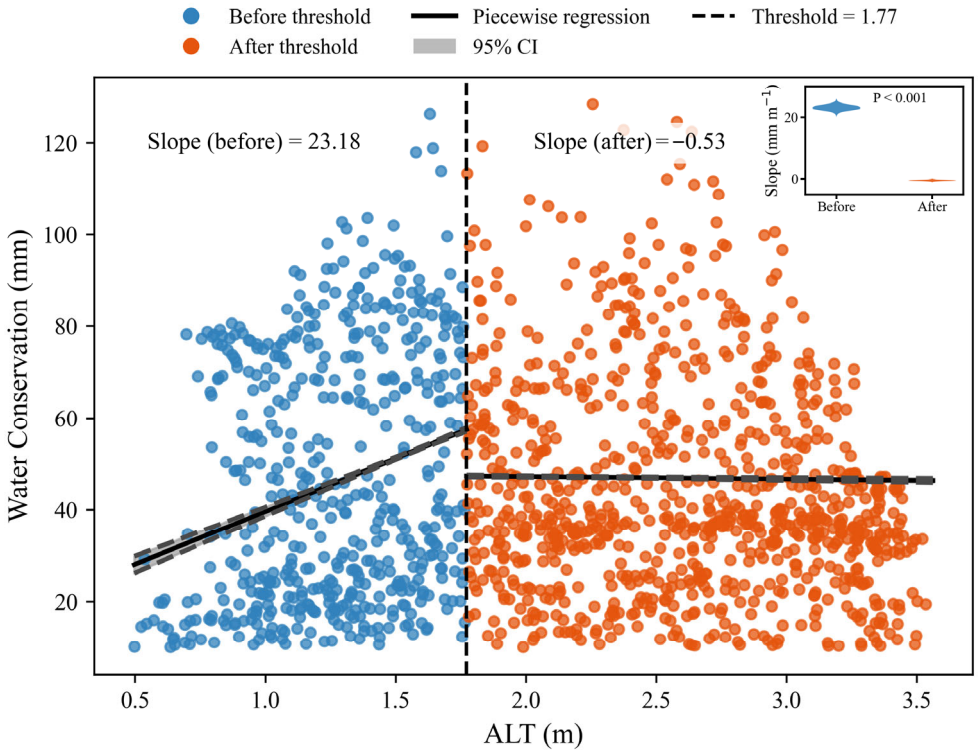

Figure 8. Piecewise linear relationship between ALT and water conservation in the TRSR.

This is consistent with previous findings from the QTP; for example, GRACE/GRACE-FO-based analyses and related reviews by Xiang et al. (2023) [57] reported that increased groundwater storage in some basins and suggested that the phase of progressive thaw deepening may correspond to more active subsurface recharge and storage. Meanwhile, our finding that gains do not persist beyond the threshold is also consistent with stage-dependent evidence in the literature: Andresen et al. (2020) [53], through multi-model comparisons, found that active layer deepening is negatively correlated with near-surface soil moisture under many scenarios, emphasizing that enhanced deep drainage and leakage may promote surface drying. Liljedahl et al. (2016) [58] further noted from observations along an ice-wedge degradation sequence that degradation may evolve from "initial drainage" to "enhanced through connectivity" and then to "landscape-scale integrated drainage," thereby reducing surface ponding and reshaping the water balance. Compared with prior work that has more often emphasized enhanced

groundwater connectivity and fluxes under degradation, the threshold region identified here—where water conservation in permafrost areas shifts from increasing storage to increasing drainage at ALT ≈ 1.77 m—provides a more testable quantitative reference for explaining nonlinear and regionally differentiated impacts of permafrost degradation on water conservation.

Cross-correlation analysis indicates a clear lagged response of the water conservation function to changes in ALT in the TRSR. The absolute correlation between ALT and the water conservation function reaches its maximum at a lag of ~5–7 years ($p < 0.05$; Figure 9a), indicating that the impacts of permafrost degradation on watershed hydrological processes are delayed and persistent. This lag effect was further quantified using a DLM. Ridge and Almon estimates show broadly consistent overall patterns and largely fall within the confidence intervals: at early lags (0–3 years), lag coefficients for ALT are generally negative and then gradually approach zero and become slightly positive, stabilizing after ~6–10 years (Figure 9b). The cumulative effect indicates that with increasing lag time, the net influence of increasing ALT on the water conservation function strengthens progressively and peaks at lags of 8–10 years (Figure 9c), reflecting lagged and cumulative impacts of permafrost degradation on watershed hydrology.

These results indicate that time lag is another important feature of how permafrost degradation affects the water conservation function. Previous studies have reported similar patterns. Rushworth et al. (2013) [48] found that the strongest response of the water conservation function to ALT changes occurs at a lag of ~5–7 years, with the cumulative effect stabilizing after ~8–10 years, indicating a pronounced "permafrost hydrological memory." Multi-model comparisons by Andresen et al. (2020) [53] suggest that climate-change forcing on soil moisture and runoff in permafrost regions is often released gradually over timescales of several to more than ten years. Permafrost degradation on the QTP is jointly driven by multi-year "climate memory" in temperature and precipitation [17]. This memory effect can be attributed to the superposition of several processes, including (i) slow heat conduction within the soil column, (ii) the time required for reorganization of storage and recharge patterns in the permafrost–groundwater system, and (iii) biological lags associated with vegetation succession under new hydrothermal conditions [59–62]. Overall, the relationship between permafrost degradation based on ALT increase and the water conservation function exhibits pronounced nonlinearity and time-lag effects. Overall, the relationship between permafrost degradation (active layer deepening) and the water conservation function exhibits pronounced nonlinearity and time-lag effects.

Under shallow active layer conditions, moderate thickening may increase effective porosity and permeability in near-surface soils and improve post-freeze–thaw soil structure, allowing a larger fraction of spring snowmelt and summer rainfall to infiltrate into the upper and mid-soil horizons. This process can temporarily increase soil water content and baseflow recharge, resulting in a bounded enhancement of the water conservation function and a characteristic "early degradation-modest increases in runoff and soil water" response [17,63]. As the active layer continues to deepen and the underlying ice-rich permafrost thaws or even disappears, deep pore connectivity increases markedly, subsurface drainage pathways open, and soil water storage capacity declines; consequently, regional hydrological processes gradually shift from "shallow storage-local runoff" to "deep drainage-regional baseflow" [64]. Numerical simulations by Bense et al. (2012) [54] and Diak et al. (2023) [65] indicate that a downward shift of the permafrost table can hydraulically connect surface water and groundwater, manifested as deepening baseflow source areas, lengthened flow paths, and lowered shallow water tables. Ma et al. (2022) [66] similarly reported in the Yellow River headwaters that in degraded permafrost zones, the

proportion of winter baseflow increases, intra-annual runoff dynamics become smoother, dry-season discharge increases, and flood-season peaks are dampened.

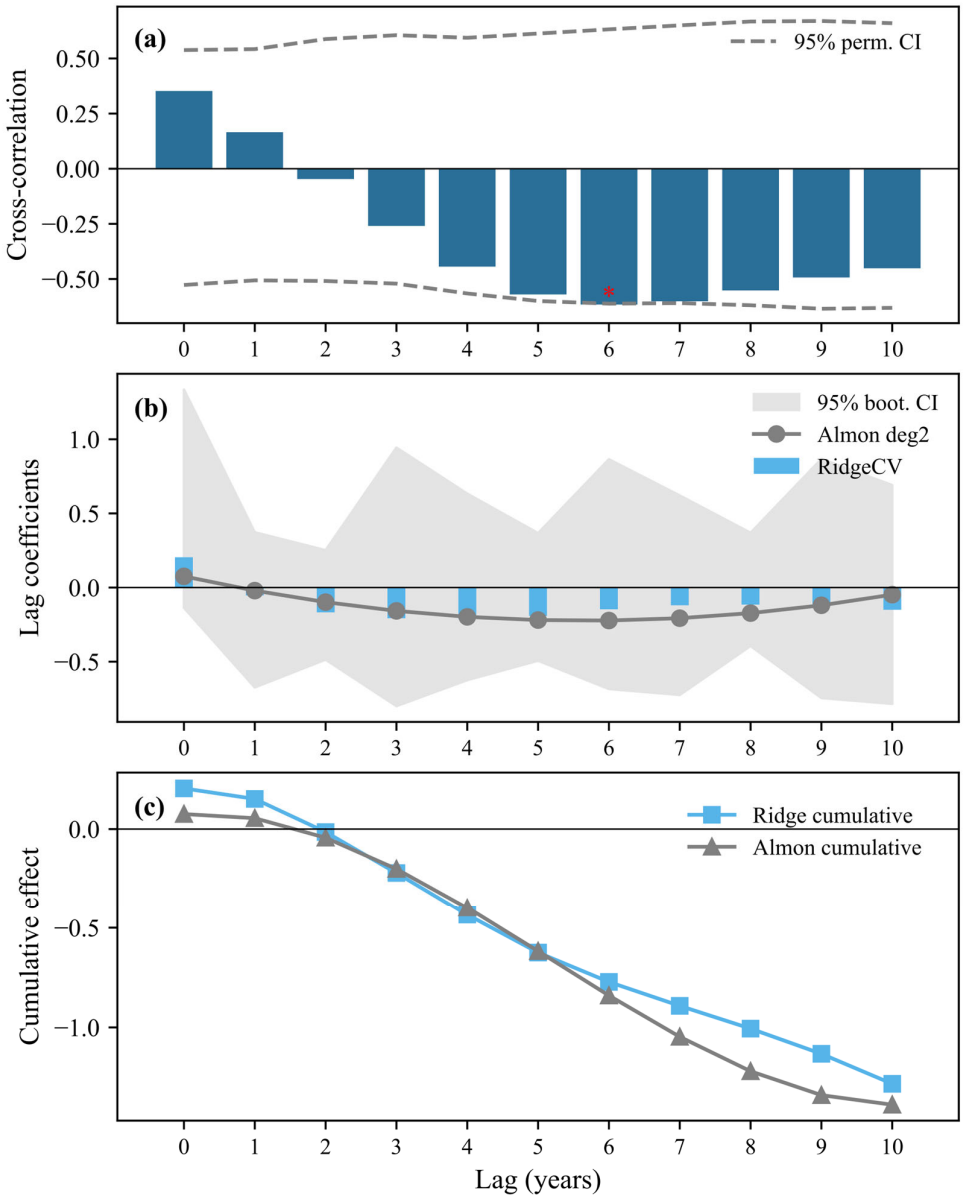

Figure 9. (**a**) Cross-correlation between detrended and standardized ALT and annual water conservation for lags 0–10 years (ALT leading). Dashed lines indicate the 95% empirical confidence interval estimated from 500 block-permutation samples (block size = 3); the red asterisk marks correlations that fall outside this interval; (**b**) DLM coefficients of water conservation response to ALT anomalies at lags 0–10 years, estimated using Ridge regression (blue bars) and a second-order Almon polynomial (gray line). The gray shading denotes 95% block-bootstrap confidence intervals for the distributed-lag coefficients (500 resamples), providing a reference for the Ridge and Almon estimates; (**c**) cumulative effects from the Ridge and Almon specifications (sum of lag coefficients), representing the net multi-year response of water conservation to a one-standard-deviation increase in ALT.

4.3. Uncertainties and Future Perspectives

The changes in water conservation capacity quantified in this study are based on existing permafrost, climate, and vegetation data products and an annual-scale InVEST framework. Because the InVEST water conservation model is grounded in long-term mean water balance, it cannot accurately capture seasonal freeze–thaw processes, snow/ice-melt recharge, or transient infiltration controls imposed by frozen ground; moreover,

ALT and permafrost distribution datasets may be affected by modeling uncertainty and scale mismatch. ALT-based permafrost degradation integrates basin-scale effects and may also be locally influenced by human activities, making strict separation challenging to separate from climatic forcing. In addition, constraints from a single (or a limited number of) gauging station(s) primarily reflect catchment-scale water balance and may not fully represent sub-basin heterogeneity. Therefore, the threshold and lag effects identified for the influence of ALT on water conservation capacity are subject to uncertainty.

Future work should deploy and integrate higher-resolution monitoring networks of ground temperature, ALT, soil moisture, and river baseflow in key permafrost areas in and around the TRSR. Remote sensing retrievals should be combined with in situ observations to improve spatiotemporal characterization of permafrost degradation and hydrological responses, thereby providing more robust data for model calibration and mechanistic testing. In parallel, remote sensing indicators such as thermokarst lake surface temperature can be incorporated into monitoring and scenario projection frameworks to characterize changes in land surface energy and water exchanges under thermokarst processes [67]. Scenario simulations under different climate conditions should also be strengthened. By considering alternative warming trajectories and human activity scenarios, future research should systematically assess how water conservation function in the TRSR may evolve over coming decades and its implications for downstream runoff processes and water security, identify risks and opportunities for key water source areas and important ecological function zones, and further examine synergies and tradeoffs between changes in water conservation function and other ecosystem services under permafrost degradation. These efforts will provide a more integrated scientific basis for ecosystem conservation and water resource management on the QTP and in alpine/cold regions worldwide.

5. Conclusions

In this study, spatiotemporal changes in water conservation across the Three-River Source Region from 1990 to 2020 were quantified using multi-source remote sensing and in situ observations combined with the InVEST water-yield framework. The influence of permafrost degradation, represented by active layer thickness (ALT), on water conservation was further examined by assessing spatial heterogeneity, time-lagged responses, and potential threshold behavior using complementary statistical analyses. The main findings are summarized as follows:

(1) During 1990–2020, water conservation in the TRSR increased overall, with the most pronounced increase in the Yangtze headwaters. Precipitation and its interaction with ALT were key drivers of spatial variability and inter-annual dynamics in water conservation.

(2) Permafrost degradation was characterized primarily by sustained ALT deepening (approximately +0.32 cm a^{-1}), and its influence on water conservation exhibited pronounced spatial non-stationarity. The effect was generally promotive in the warm–humid southeast but weakened and even became negative in the cold–dry northwest. Moreover, the response was nonlinear, and ALT approaching ~1.77 m may trigger a structural shift in hydrological processes, indicating a potential threshold response.

(3) Water conservation in the TRSR showed a significant lagged response to ALT changes: the absolute correlation peaked when ALT led by 5–7 years ($p < 0.05$), and cumulative effects strengthened with increasing lag and stabilized after reaching a maximum at 8–10 years, indicating a pronounced "permafrost hydrological memory."

From the perspectives of long-term time series and spatial non-stationarity, this study elucidates the coupled mechanism among "water conservation–precipitation–ALT change" in the TRSR, together with its threshold and lag-response characteristics, thereby providing

key evidence for water security assessment, ecological engineering optimization, and adaptive management in permafrost-sensitive regions.

Supplementary Materials: The following supporting information can be downloaded at: https://www.mdpi.com/article/10.3390/rs18040623/s1, Table S1: Robustness test of permafrost (ALT) effects under ±0.05 m ALT uncertainty (GeoDetector, pooled 1990–2020 sample).

Author Contributions: Conceptualization, W.B., C.W., W.L., Q.W. and Z.G.; Methodology, W.B., C.W., Y.Y. and Z.G.; Software, W.B.; Validation, C.W., G.Z. and Q.W.; Formal analysis, W.L. and Z.G.; Investigation, G.Z. and Y.Y.; Resources, C.W.; Data curation, W.L., G.Z. and Q.W.; Writing—original draft preparation, W.B., C.W., W.L., Q.W. and Z.G.; Writing—review and editing, W.B., C.W., W.L., Q.W., G.Z., Y.Y. and Z.G.; Visualization, C.W., W.L. and Y.Y.; Supervision, W.B. and Z.G.; Project administration, W.B. and Z.G.; Funding acquisition, W.B. and Z.G. All authors have read and agreed to the published version of the manuscript.

Funding: This research was funded by the Science Fund for Distinguished Young Scholars of Gansu Province (Grant No. 25JRRA489), the National Science Foundation of China (Grant No. 42371150), the Youth Innovation Promotion Association of the Chinese Academy of Sciences (Grant No. 2023445), the Natural Science Foundation of Gansu Province (Grant No. 25JRRA166), and the Department of Education of Gansu Province: Major Cultivation Project of Scientific Research Innovation Platform in University (Grant No. 2024CXPT-14).

Data Availability Statement: The model and the data that support the findings of this study are available upon reasonable request from the corresponding author.

Acknowledgments: The authors are grateful to the academic editor and the anonymous reviewers for their constructive comments and helpful suggestions.

Conflicts of Interest: The authors declare no conflicts of interest.

References

1. Brauman, K.A.; Daily, G.C.; Duarte, T.K.; Mooney, H.A. The nature and value of ecosystem services: An overview highlighting hydrologic services. *Annu. Rev. Environ. Resour.* **2007**, *32*, 67–98. [CrossRef]
2. Wang, P.; Xu, M. Dynamics and interactions of water-related ecosystem services in the Yellow River Basin, China. *J. Geogr. Sci.* **2023**, *33*, 1681–1701. [CrossRef]
3. Vörösmarty, C.J.; McIntyre, P.B.; Gessner, M.O.; Dudgeon, D.; Prusevich, A.; Green, P.; Glidden, S.; Bunn, S.E.; Sullivan, C.A.; Liermann, C.R.; et al. Global threats to human water security and river biodiversity. *Nature* **2010**, *467*, 555–561. [CrossRef] [PubMed]
4. Yu, C.; Duan, P.; Yu, Z.; Gao, B. Experimental and model investigations of vegetative filter strips for contaminant removal: A review. *Ecol. Eng.* **2019**, *126*, 25–36. [CrossRef]
5. Mayer, P.M.; Reynolds, S.K., Jr.; McCutchen, M.D.; Canfield, T.J. Meta-analysis of nitrogen removal in riparian buffers. *J. Environ. Qual.* **2007**, *36*, 1172–1180. [CrossRef]
6. Millennium Ecosystem Assessment. *Millennium Ecosystem Assessment*; Millennium Ecosystem Assessment: Washington, DC, USA, 2001.
7. Cheng, G.; Jin, H. Permafrost and groundwater on the Qinghai-Tibet Plateau and in northeast China. *Hydrogeol. J.* **2013**, *21*, 5–23. [CrossRef]
8. Cao, W.; Wu, D.; Huang, L.; Liu, L. Spatial and temporal variations and significance identification of ecosystem services in the Sanjiangyuan National Park, China. *Sci. Rep.* **2020**, *10*, 6151. [CrossRef]
9. Pan, Y.; Yin, Y. Spatial and temporal evolution characteristics of water conservation in the Three-Rivers Headwater Region and the driving factors over the past 30 years. *Atmosphere* **2023**, *14*, 1453. [CrossRef]
10. People's Daily Online. Sanjiangyuan National Park Serves as Vivid Exemplar of China's National Park System. Available online: https://en.people.cn/n3/2022/0902/c90000-10143002.html (accessed on 4 June 2025).
11. Yang, Y.; Chen, R.; Ding, Y.; Zhao, Q.; Li, H.; Liu, Z. Variation in the hydrological cycle in the Three-River Headwaters Region based on multi-source data. *Front. Environ. Sci.* **2022**, *10*, 1088467. [CrossRef]
12. Hu, J.; Nan, Z.; Ji, H. Spatiotemporal characteristics of NPP changes in frozen ground areas of the Three-River Headwaters region, China: A regional modeling perspective. *Front. Earth Sci.* **2022**, *10*, 838558. [CrossRef]

13. Walvoord, M.A.; Kurylyk, B.L. Hydrologic impacts of thawing permafrost-A review. *Vadose Zone J.* **2016**, *15*, vzj2016.01.0010. [CrossRef]
14. Schuur, E.A.G.; McGuire, A.D.; Schädel, C.; Grosse, G.; Harden, J.W.; Hayes, D.J.; Hugelius, G.; Koven, C.D.; Kuhry, P.; Lawrence, D.M.; et al. Climate change and the permafrost carbon feedback. *Nature* **2015**, *520*, 171–179. [CrossRef] [PubMed]
15. Jin, X.; Jin, H.; Wu, X.; Luo, D.; Yu, S.; Li, X.; He, R.; Wang, Q.; Knops, J.M.H. Permafrost degradation leads to biomass and species richness decreases on the northeastern Qinghai-Tibet Plateau. *Plants* **2020**, *9*, 1453. [CrossRef] [PubMed]
16. Jiang, C.; Li, D.; Wang, D.; Zhang, L. Quantification and assessment of changes in ecosystem service in the Three-River Headwaters Region, China as a result of climate variability and land cover change. *Ecol. Indic.* **2016**, *66*, 199–211. [CrossRef]
17. Zhang, F.; Li, H.; Luo, F.; Wang, C.; Wang, J.; Ma, W.; Yang, Y.; Li, Y. Evaluations on topsoil water storage and water conservation capacity of the Sanjiangyuan National Park based on boosted regression trees. *Chin. J. Ecol.* **2022**, *41*, 2471.
18. Gao, H.; Wang, J.; Yang, Y.; Pan, X.; Ding, Y.; Duan, Z. Permafrost hydrology of the Qinghai-Tibet Plateau: A review of processes and modeling. *Front. Earth Sci.* **2021**, *8*, 576838. [CrossRef]
19. Lv, M.; Wang, Y.; Gao, Z. The change process of soil hydrological properties in the permafrost active layer of the Qinghai-Tibet Plateau. *CATENA* **2022**, *210*, 105938. [CrossRef]
20. Jin, X.; Jin, H.; Luo, D.; Sheng, Y.; Wu, Q.; Wu, J.; Wang, W.; Huang, S.; Li, X.; Liang, S.; et al. Impacts of permafrost degradation on hydrology and vegetation in the source area of the Yellow River on Northeastern Qinghai-Tibet Plateau, Southwest China. *Front. Earth Sci.* **2022**, *10*, 845824. [CrossRef]
21. Yang, Y.; Wu, Q.; Jin, H.; Wang, Q.; Huang, Y.; Luo, D.; Gao, S.; Jin, X. Delineating the hydrological processes and hydraulic connectivities under permafrost degradation on Northeastern Qinghai-Tibet Plateau, China. *J. Hydrol.* **2019**, *569*, 359–372. [CrossRef]
22. Dongdong, C.; Qi, L.; Lili, H.; Qian, X.; Xin, C.; Fuquan, H.; Liang, Z. Soil nutrients directly drive soil microbial biomass and carbon metabolism in the sanjiangyuan alpine grassland. *J. Soil Sci. Plant Nutr.* **2023**, *23*, 3548–3560. [CrossRef]
23. Su, T.; Miao, C.; Duan, Q.; Gou, J.; Guo, X.; Zhao, X. Hydrological response to climate change and human activities in the Three-River Source Region. *Hydrol. Earth Syst. Sci. Discuss.* **2022**, *2022*, 1477–1492. [CrossRef]
24. Wang, J.; Sun, H.; Xiong, J.; He, D.; Cheng, W.; Ye, C.; Yong, Z.; Huang, X. Dynamics and drivers of vegetation phenology in three-river headwaters region based on the Google Earth Engine. *Remote Sens.* **2021**, *13*, 2528. [CrossRef]
25. Xiao, Z.; Ding, M.; Li, L.; Nie, Y.; Pan, J.; Li, R.; Liu, L.; Zhang, Y. Divergent changes of surface water and its climatic drivers in the headwater region of the Three Rivers on the Qinghai-Tibet Plateau. *Ecol. Indic.* **2024**, *158*, 111615. [CrossRef]
26. Zhai, X.; Liang, X.; Yan, C.; Xing, X.; Jia, H.; Wei, X.; Feng, K. Vegetation dynamic changes and their response to ecological engineering in the Sanjiangyuan Region of China. *Remote Sens.* **2020**, *12*, 4035. [CrossRef]
27. Liu, J.; Xu, X.; Shao, Q. Grassland degradation in the "three-river headwaters" region, Qinghai province. *J. Geogr. Sci.* **2008**, *18*, 259–273. [CrossRef]
28. Bai, Y.; Guo, C.; Degen, A.A.; Ahmad, A.A.; Wang, W.; Zhang, T.; Li, W.; Ma, L.; Huang, M.; Zeng, H.; et al. Climate warming benefits alpine vegetation growth in Three-River Headwater Region, China. *Sci. Total Environ.* **2020**, *742*, 140574. [CrossRef]
29. Zou, D.; Zhao, L.; Sheng, Y.; Chen, J.; Hu, G.; Wu, T.; Wu, J.; Xie, C.; Wu, X.; Pang, Q.; et al. A new map of permafrost distribution on the Tibetan Plateau. *Cryosphere* **2017**, *11*, 2527–2542. [CrossRef]
30. Zhou, F.; Yao, M.; Fan, X.; Yin, G.; Meng, X.; Lin, Z. Evidence of warming from long-term records of climate and permafrost in the hinterland of the Qinghai-Tibet Plateau. *Front. Environ. Sci.* **2022**, *10*, 836085. [CrossRef]
31. The Natural Capital Project. InVEST User Guide (Integrated Valuation of Ecosystem Services and Tradeoffs). Available online: https://storage.googleapis.com/releases.naturalcapitalproject.org/invest-userguide/latest/en/index.html (accessed on 4 June 2025).
32. Peng, S.; Ding, Y.; Liu, W.; Li, Z. 1 km monthly temperature and precipitation dataset for China from 1901 to 2017. *Earth Syst. Sci. Data* **2019**, *11*, 1931–1946. [CrossRef]
33. Peng, S. *1 km Monthly Potential Evapotranspiration Dataset in China (1901–2024)*; National Tibetan Plateau Data Center: Beijing, China, 2022. Available online: https://www.tpdc.ac.cn/zh-hans/data/8b11da09-1a40-4014-bd3d-2b86e6dccad4/ (accessed on 4 January 2025).
34. Yang, J.; Huang, X. 30 m annual land cover and its dynamics in China from 1990 to 2019. *Earth Syst. Sci. Data Discuss.* **2021**, *2021*, 3907–3925. [CrossRef]
35. Wei, Y. *The Boundaries of the Source Regions in Sanjiangyuan Region*; National Tibetan Plateau Data Center: Beijing, China, 2018. Available online: https://www.escience.org.cn/metadata/detail?cstrId=CSTR%3A18406.11.Geogra.tpdc.270009&id=da0e21dd01bcbea6d33bd0c6ce9c2c33%3AGeogra.tpdc.270009 (accessed on 5 January 2025).
36. Yan, D.; Zheng, X.; Feng, M.; Liang, S.; Hu, Z.; Kuang, X.; Feng, Y. *Frozen Ground Change Data Set in the Tibetan Plateau (1961–2020)*; National Tibetan Plateau Data Center: Tibet, China, 2024. Available online: https://data.tpdc.ac.cn/en/data/51ce7562-b3cb-4fca-88b5-dc750845e857 (accessed on 5 January 2025).

37. Yan, F.; Shangguan, W.; Zhang, J.; Hu, B. Depth-to-bedrock map of China at a spatial resolution of 100 m. *Sci. Data* **2020**, *7*, 2. [CrossRef]
38. Hengl, T.; Mendes de Jesus, J.; Heuvelink, G.B.M.; Ruiperez Gonzalez, M.; Kilibarda, M.; Blagotić, A.; Shangguan, W.; Wright, M.N.; Geng, X.; Bauer-Marschallinger, B.; et al. SoilGrids250m: Global gridded soil information based on machine learning. *PLoS ONE* **2017**, *12*, e0169748. [CrossRef] [PubMed]
39. Song, X. *Dataset of Vegetation Index, Albedo and Land Surface Temperature on the Qinghai-Tibet Plateau (1981–2020)*; National Tibetan Plateau Data Center: Tibet, China, 2023. Available online: https://www.gscloud.cn/qtp/qtpecosys/dataset/dataset_detail/b61ae6e84e444b1597b8dddfffe9c1f3 (accessed on 6 January 2025).
40. Li, M.; Liang, D.; Xia, J.; Song, J.; Cheng, D.; Wu, J.; Cao, Y.; Sun, H.; Li, Q. Evaluation of water conservation function of Danjiang River Basin in Qinling Mountains, China based on InVEST model. *J. Environ. Manag.* **2021**, *286*, 112212. [CrossRef] [PubMed]
41. Tibetan Plateau Vegetation Indices, Albedo and Land Surface Temperature Dataset (1981–2020). Available online: https://data.tpdc.ac.cn/zh-hans/data/f1817320-124b-4633-9309-0f20125e276f (accessed on 15 January 2026).
42. Yao, J.; Yi, C.-L.; Fu, P. Evaluation of the Accuracy of SRTM3 and ASTER GDEM in the Tibetan Plateau Mountain Ranges. *E3S Web Conf.* **2020**, *206*, 01027. [CrossRef]
43. Fu, B. On the calculation of evaporation from land surface. *Chin. J. Atmos. Sci.* **1981**, *5*, 23–31.
44. Wheeler, D.; Tiefelsdorf, M. Multicollinearity and correlation among local regression coefficients in geographically weighted regression. *J. Geogr. Syst.* **2005**, *7*, 161–187. [CrossRef]
45. Wang, J.-F.; Li, X.-H.; Christakos, G.; Liao, Y.-L.; Zhang, T.; Gu, X.; Zheng, X.-Y. Geographical detectors-based health risk assessment and its application in the neural tube defects study of the Heshun Region, China. *Int. J. Geogr. Inf. Sci.* **2010**, *24*, 107–127. [CrossRef]
46. McMillen, D.P. Geographically weighted regression: The analysis of spatially varying relationships. *Am. J. Agric. Econ.* **2004**, *86*, 554–556. [CrossRef]
47. Huang, H.; Wang, Z.; Xia, F.; Shang, X.; Liu, Y.; Zhang, M.; Dahlgren, R.A.; Mei, K. Water quality trend and change-point analyses using integration of locally weighted polynomial regression and segmented regression. *Environ. Sci. Pollut. Res.* **2017**, *24*, 15827–15837. [CrossRef]
48. Rushworth, A.M.; Bowman, A.W.; Brewer, M.J.; Langan, S.J. Distributed lag models for hydrological data. *Biometrics* **2013**, *69*, 537–544. [CrossRef]
49. Tao, J.; Zhang, J.; Guo, L.; Wang, J.; Xue, H. Spatiotemporal change and driving factors of water conservation in Sanjiangyuan National Park. *Acta Ecol. Sin.* **2025**, *45*, 1226–1238.
50. Han, P.; Yang, G.; Liu, Y.; Chen, X.; Wen, Z.; Shi, H.; Hu, E.; Xue, T.; Zhao, Y. Vegetation Restoration Enhanced Canopy Interception and Soil Evaporation but Constrained Transpiration in Hekou-Longmen Section During 2000–2018. *Agronomy* **2024**, *14*, 2606. [CrossRef]
51. Qiu, D.; Xu, R.; Wu, C.; Mu, X.; Zhao, G.; Gao, P. Vegetation restoration improves soil hydrological properties by regulating soil physicochemical properties in the Loess Plateau, China. *J. Hydrol.* **2022**, *609*, 127730. [CrossRef]
52. Caviedes-Voullième, D.; Ahmadinia, E.; Hinz, C. Interactions of microtopography, slope and infiltration cause complex rainfall-runoff behavior at the hillslope scale for single rainfall events. *Water Resour. Res.* **2021**, *57*, e2020WR028127. [CrossRef]
53. Andresen, C.G.; Lawrence, D.M.; Wilson, C.J.; Wilson, C.J.; McGuire, A.D.; Koven, C.; Schaefer, K.; Jafarov, E.; Peng, S.; Chen, X.; et al. Soil moisture and hydrology projections of the permafrost region-a model intercomparison. *Cryosphere* **2020**, *14*, 445–459. [CrossRef]
54. Errington, R.C.; Macdonald, S.E.; Bhatti, J.S. Rate of permafrost thaw and associated plant community dynamics in peatlands of northwestern Canada. *J. Ecol.* **2024**, *112*, 1565–1582. [CrossRef]
55. Wang, X.; Chen, R.; Yang, Y. Effects of permafrost degradation on the hydrological regime in the source regions of the Yangtze and Yellow Rivers, China. *Water* **2017**, *9*, 897. [CrossRef]
56. Qin, J.; Ding, Y.; Han, T.; Chang, Y.; Shi, F.; You, Y. The hydrothermal changes of permafrost active layer and their impact on summer rainfall-runoff processes in an alpine meadow watershed, northwest China. *Res. Cold Arid Reg.* **2022**, *14*, 361–369. [CrossRef]
57. Xiang, L.; Wang, H.; Steffen, H.; Jiang, L.; Shen, Q.; Jia, L.; Su, Z.; Wang, W.; Deng, F.; Qiao, B.; et al. Two decades of terrestrial water storage changes in the tibetan plateau and its surroundings revealed through GRACE/GRACE-FO. *Remote Sens.* **2023**, *15*, 3505. [CrossRef]
58. Liljedahl, A.K.; Boike, J.; Daanen, R.P.; Fedorov, A.N.; Frost, G.V.; Grosse, G.; Hinzman, L.D.; Iijma, Y.; Jorgen-son, J.C.; Matveyeva, N.; et al. Pan-Arctic ice-wedge degradation in warming permafrost and its influence on tundra hydrology. *Nat. Geosci.* **2016**, *9*, 312–318. [CrossRef]
59. Ding, K.; Jiang, P.; Ni, J.; Shen, T.; Yang, B.; Zhang, R.; Yu, Z. Machine learning uncovers a multi-year climate memory in permafrost degradation on the Qinghai-Tibet Plateau: The critical roles of precipitation and lagged temperature. *J. Hydrol.* **2025**, *663*, 134272. [CrossRef]

60. Romanovsky, V.E.; Osterkamp, T.E. Effects of unfrozen water on heat and mass transport processes in the active layer and permafrost. *Permafrost Periglac. Process.* **2000**, *11*, 219–239. [CrossRef]
61. Bense, V.F.; Kooi, H.; Ferguson, G.; Read, T. Permafrost degradation as a control on hydrogeological regime shifts in a warming climate. *J. Geophys. Res. Earth Surf.* **2012**, *117*, F3. [CrossRef]
62. Watts, K.; Whytock, R.C.; Park, K.J.; Fuentes-Montemayor, E.; Macgregor, N.A.; Duffield, S.; McGowan, P.J.K. Ecological time lags and the journey towards conservation success. *Nat. Ecol. Evol.* **2020**, *4*, 304–311. [CrossRef] [PubMed]
63. Suzuki, K.; Park, H.; Makarieva, O.; Kanamori, H.; Hori, M.; Matsuo, K.; Matsumura, S.; Nesterova, N.; Hiyama, T. Effect of permafrost thawing on discharge of the Kolyma River, Northeastern Siberia. *Remote Sens.* **2021**, *13*, 4389. [CrossRef]
64. Gao, Z.; Yin, G.; Niu, F.; Wang, Y.; Luo, J.; Lin, Z.; Shang, Y.; Zhang, C.; Liu, W. Dynamics and drivers of suprapermafrost groundwater on the Qinghai-Tibet Plateau under climate change. *Water Resour. Res.* **2025**, *61*, e2025WR040246. [CrossRef]
65. Diak, M.; Böttcher, M.E.; von Ahn, C.M.E.; Hong, W.-L.; Kędra, M.; Kotwicki, L.; Koziorowska-Makuch, K.; Kuliński, K.; Lepland, A.; Makuch, P.; et al. Permafrost and groundwater interaction: Current state and future perspective. *Front. Earth Sci.* **2023**, *11*, 1254309. [CrossRef]
66. Ma, Q.; Jin, H.-J.; Bense, V.F.; Luo, D.-L.; Marchenko, S.S.; Harris, S.A.; Lan, Y.-C. Impacts of degrading permafrost on streamflow in the source area of Yellow River on the Qinghai-Tibet Plateau, China. *Adv. Clim. Change Res.* **2020**, *10*, 225–239. [CrossRef]
67. Zhang, C.; Gao, Z.; Luo, J.; Liu, W.; Chen, M.; Niu, F.; Wang, Y.; Shang, Y. Simulation and Prediction of Thermokarst Lake Surface Temperature Changes on the Qinghai-Tibet Plateau. *Remote Sens.* **2024**, *16*, 4645. [CrossRef]

Disclaimer/Publisher's Note: The statements, opinions and data contained in all publications are solely those of the individual author(s) and contributor(s) and not of MDPI and/or the editor(s). MDPI and/or the editor(s) disclaim responsibility for any injury to people or property resulting from any ideas, methods, instructions or products referred to in the content.